Sustainable Energy & Fuels

ROYAL SOCIETY OF CHEMISTRY

PAPER

View Article Online
View Journal | View Issue

Cite this: *Sustainable Energy Fuels*, 2022, **6**, 2835

Inverted organic photovoltaics with a solution-processed Mg-doped ZnO electron transport layer annealed at 150 °C†‡

Ioannis Ierides, [a] Giovanni Ligorio, [b] Martyn A. McLachlan, [c] Kunping Guo, [a] Emil J. W. List-Kratochvil [bd] and Franco Cacialli *[a]

The use of dopants is an effective strategy to improve ZnO electron transport layers (ETLs) for application in solution-processed opto-electronic devices. Mg, in particular, has shown significant promise as a dopant and Mg-doped ZnO ETLs have been used to enhance the performance of a number of solution-processed light-emitting diodes and photovoltaics. However, such a use of Mg to dope ZnO ETLs for organic photovoltaics (OPVs) has remained limited, and only investigated in connection with annealing temperatures of 300 °C or so. In this work, with a view to increase sustainability and compatibility with soft and flexible or foldable substrates, we present OPVs incorporating Mg-doped ZnO ETLs fabricated with annealing temperatures of 150 °C. We demonstrate that Mg doping (≈1% at%) in the ZnO ETL reduces leakage currents and recombination losses in our devices, whilst leaving the morphology of the active layer and the work function of the ETL unaffected. A concomitant increase of the short circuit current density, open circuit voltage and fill factor is also observed, thereby leading to a relative enhancement of the power conversion efficiency by ≈18% compared to devices prepared using undoped ZnO.

Received 15th December 2021
Accepted 10th April 2022

DOI: 10.1039/d1se02001c

rsc.li/sustainable-energy

Introduction

Solution-processed optoelectronics can offer cheap fabrication over large areas. To fully realise this attractive potential, it is essential to avoid high temperature processing of their various device components.[1] Low temperature processing allows for significant energy savings that makes manufacturing more sustainable[2] and reduces cost that can, in turn, lower the barriers to market entry.[3] For the case of organic semiconductors (OS) in particular, a key opportunity to penetrate the market is *via* niche applications[4,5] which in turn usually require the use of flexible substrates.[6] In most cases such substrates are not compatible with "high temperatures" (*i.e.* >150 °C). While OS can be processed effectively at temperatures below 150 °C,[7] other essential device components require high temperature processing, as in the case of certain electron transport layers (ETLs). The use of ETLs confers many advantages, including the reduction of recombination losses between the electrode and active layer, *via* the formation of an ohmic contact.[8–12] Metal oxides are very attractive ETLs as they exhibit high optical transparency and good electron transport properties. However, to achieve long-term stability, metal oxide ETLs frequently require high temperature treatment. For some applications, such as internet of things (IOT) devices that can be used to power smart packaging on supermarket shelfs, a long lifetime may not be required. In other cases where long lifetimes are necessary, judicious selection and engineering of the precursor materials or techniques such as UV-ozone treatment[13] have shown promise in prolonging the lifetime of devices based on metal oxide ETLs processed at low temperatures.

ZnO is one of the most widely used metal oxide ETLs,[14] especially in the case of organic photovoltaics (OPVs).[15] There are a number of routes that enable the formation of a ZnO ETL such as atomic layer deposition,[16] pulsed laser deposition,[17] metal organic chemical vapor deposition,[18] spray pyrolysis and electrodeposition[19] but in most reports the facile sol–gel spin-coating method is used.[20,21] Sol–gel ZnO has shown great promise as a low temperature processed metal oxide with reasonable stability. For example, Sun *et al.* fabricated devices using ZnO ETLs processed at 130 and 150 °C that retained 70% of the power conversion efficiency (PCE) after exposure in air at room temperature for more than 30 days and without

[a]*Department of Physics and Astronomy and London Centre for Nanotechnology, University College London, London, WC1E 6BT, UK. E-mail: f.cacialli@ucl.ac.uk; Tel: +44 (0)20 7679 4467*

[b]*Institut für Physik, Institut für Chemie & IRIS Adlershof, Humboldt-Universität zu Berlin, Zum Großen Windkanal 2, Berlin 12489, Germany*

[c]*Department of Materials and Centre for Processable Electronics, Molecular Science Research Hub, Imperial College, London W12 0BZ, UK*

[d]*Helmholtz-Zentrum Berlin für Materialien und Energie GmbH, Hahn-Meitner-Platz 1, Berlin 14109, Germany*

† Dedicated in memory of Alasdair J. Campbell.

‡ Electronic supplementary information (ESI) available. See https://doi.org/10.1039/d1se02001c

encapsulation.[22] In addition, low-temperature processed ZnO ETLs have been reported to outperform (in terms of PCE) ZnO ETLs annealed at higher temperatures.[23–25] Nevertheless, sol–gel ZnO drawbacks include a poor interfacial contact with the bulk heterojunction active layer and surface defects that can act as electron trap sites and thus affect device performance. In addition, given the large number of different acceptor materials that have been developed for use in active layers of OPVs,[5] having some degree of control over the properties of the ZnO ETL such as its work function or conductivity, so as to tailor it for the specific active layer blend has become crucial. To this end, three main strategies have been developed over time to remedy the shortcomings of ZnO ETLs and to enable control of its properties. One possibility is the treatment of the deposited ZnO with UV-ozone.[13,26] We incidentally note that this is similar to oxygen-plasma treatments that are usually applied to indium-tin oxide (ITO) electrodes to increase their work function, smooth surfaces and increase their surface polarity.[27] UV-ozone treatment can also adjust a layer's work function thereby potentially allowing better energy level alignment when required. Another effective strategy is to apply a modifying interlayer between ZnO and the active layer.[28] However, the above processes require additional steps to obtain the final ETL. When considering the fabrication of solution-processed photovoltaics (PVs) at an industrial scale, a more streamlined approach is desirable or even required. For example, a more favourable strategy involves the direct addition of dopants in the precursor solution of the ZnO ETL so that the finalised improved ETL can be formed without the need of additional processing steps.

A number of different materials have been tested as dopants to be added to ZnO precursor solutions, and enabled formation of ETLs with superior characteristics when compared to their undoped ZnO ETL counterparts (specifically in terms of PCE of OPVs incorporating them). The list of such dopants is varied and includes, among others, organic molecules, 2-D materials, and metals. For example, Li and collaborators[29] used the organic molecule 2,3,5,6-tetrafluoro-7,7,8,8-tetracyanoquinodimethane (F4TCNQ) as dopant, and found that it suppresses the non-geminate recombination in OPVs by filling the traps in ZnO and leads to a relative increase in the PCE by ≈15%. Trap filling has also been achieved by an alternative molecular dopant TPT-S as shown by Xia *et al.*[30] Another successful organic molecule dopant for ZnO ETLs is an alcohol-soluble isoindigo derivative with thiophene groups and sulfobetaine zwitterions (IIDTh-NSB)[31] that can improve the interfacial compatibility between ZnO and the active layer. The 2-D MXene $Ti_3C_2T_X$ has also been recently used effectively as dopant in ZnO ETLs.[32] The $Ti_3C_2T_X$ nanosheets act as bridges between the ZnO nanocrystals and therefore provide additional charge transfer paths and passivate the surface of ZnO. These favourable changes lead to a relative increase in the PCE by ≈10%. Metals have also proved useful dopants for ZnO ETLs. Park, Kang & Cho[33] added aluminium to ZnO to optimise the ETL conductivity, thereby also reducing the overall cell series resistance. Au nanoparticles have instead been used by Usmani *et al.*[34] and Chi *et al.*[35] to facilitate an increase in the optical absorption of the active layer *via* exploitation of plasmonic effects. Another transition metal, zirconium, has been employed by Song *et al.*[36] to improve electron transport and transmittance of ZnO and concomitantly increase the relative PCE by ≈12%. Another recent example is the study by Wang *et al.*[37] where alkali metal salts (lithium acetate or caesium acetate) were used to dope the ZnO ETL. The study indicated an improved crystallinity of the ETL and an increased shunt resistance, leading to a reduced current leakage. The open circuit voltage (V_{OC}), fill factor (FF) and the short circuit current density (J_{SC}) increased simultaneously for the devices with ETLs containing alkali metal salts.

Having used MgO successfully to form a bilayer ETL with ZnO in previous work[28] (where a non-uniform ultrathin MgO layer ≈ 10 nm was inserted between ZnO and the active layer) we were interested to test whether direct addition of the MgO precursor to the ZnO precursor solution is a viable route to form a Mg-doped ZnO ETL for application to OPVs. Such an approach would obviously favour scalability at an industrial level, because it requires fewer steps and eliminates the need to control the MgO layer thickness to a few nm. Thickness control is in fact crucial, because we observed that MgO interlayers of ≈150 nm or so hinder performance significantly and that for an efficient device 10 nm thick (even if non-uniform) ETLs are necessary. It would be rather difficult to achieve such a layer with the required degree of accuracy and consistency in an industrial process. Hence, directly doping the ZnO layer with Mg would be advantageous over the bilayer approach as it is much easier to control the concentrations of precursor materials rather than film thickness in large scale processes.

Previous literature demonstrated how a Mg-doped ZnO ETL formed from a single solution can be employed in a variety of solution-processed devices to improve efficiency. For example, such a layer has been incorporated in quantum dot and perovskite light-emitting diodes, either on its own or in combination with another ZnO layer to inject electrons.[38–46] Such studies have demonstrated that doping ZnO with Mg can lead to a more balanced injection and therefore an increase in the maximum external quantum efficiency and current efficiency. The improvement has been attributed to a decreased conductivity and an upward shift of the conduction band of the Mg-doped ZnO ETL compared to the undoped ZnO ETL. These findings are in-line with studies investigating the optical properties of Mg-doped ZnO films and nano-particles,[47–49] which revealed that increasing the amount of Mg dopant results in an increase in the band gap of the ZnO thin film and that the work function of the Mg-doped ZnO film can be controlled based on the doping level of Mg. Sol–gel Mg-doped ZnO ETLs have also been used to improve the PCE of several PV systems. These include silicon[50] and dye-sensitised solar cells[51,52] as well as PVs based on Cu_2O,[53] quantum dots[54] and perovskites.[55,56] Since the working principle of these PV systems differs, the mechanism by which each PV system benefits from the presence of Mg dopants varies. For example, the dye-sensitised solar cells benefit from the upward shifting of the conduction band which leads to an increased V_{OC} in the devices. This and that combined with an increase of J_{SC} yields an optimised performance. For the case of perovskite absorbers, the carrier

recombination at the interface between the ETL and perovskite active layer is suppressed due to the Mg doping leading to the enhanced performance. Depending on the materials used and on the preparation protocols the amount of Mg doping necessary to form the "optimum" Mg-doped ZnO ETL varies.

The Mg-doped ZnO single layer ETL has provided excellent results in all the above systems, however, its use for OPVs has remained limited.[57] Only two works by Yin *et al.*[58] and by MacLeod *et al.*[59] have reported its application in bulk heterojunction OPVs. In both cases the Mg-doped ZnO ETL outperformed the corresponding undoped ZnO ETL in terms of PCE as a result of the reduced carrier recombination and increased charge-collection. In the case of MacLeod *et al.* blends of poly(3-hexylthiophene-2,5-diyl) (P3HT) as the donor and $PC_{70}BM$ or indene-C60 bisadduct (ICBA) as acceptors were used as active layers. The best PCE was achieved when a doping of 10 mol% (of Mg in precursor solids) was present in the ETL with the increase in PCE mainly resulting from an enhanced V_{OC} and FF. In the study by Yin *et al.* the blend used as active layer consisted of PTB7 as the donor and $PC_{70}BM$ as the acceptor. In this case the best PCE was achieved with a 30% Mg substitutional doping, (*i.e.* with $x = 0.3$ in the zinc magnesium oxide layer with formula $Zn_{1-x}Mg_xO$), with the biggest improvement observed in the J_{SC} and FF of the devices. Both of these studies are excellent demonstrations of the potential of Mg as a dopant to improve ZnO ETLs for use in OPVs. However, the annealing temperatures used to form the Mg-doped ZnO ETLs are 290 °C and 300 °C for Yin *et al.* and MacLeod *et al.* respectively. These annealing temperatures are not favourable for industrial scale applications and may not be suitable where plastic flexible substrates are mandated by the application. In addition, reducing the processing temperature automatically increases the sustainability of the whole life cycle. For this reason, we investigated whether a lower annealing temperature of 150 °C could also be applied to form Mg-doped ZnO ETLs for application in bulk heterojunction OPVs. The lower processing temperature might also allow, in principle, fabrication of the electrodes on top of an already deposited active layer without the damaging effects connected, for example, with sputtering (*e.g.* of ITO).[60]

In particular, we show that such devices can outperform OPVs containing equivalent undoped ZnO ETLs by increasing the J_{SC}, V_{OC} and FF and therefore the PCE. The best results were obtained when the ZnO ETL is doped with ≈1% of Mg. Without changing the work function of the ETL or morphology of the active layer – as verified by ultraviolet photoemission spectroscopy (UPS), Kelvin probe and atomic force microscopy (AFM) – we show that this level of Mg doping enables the formation of an improved electrode that leads to reduced recombination losses in OPV devices. This is demonstrated by measurement of the dependence of the photocurrent on the so-called "effective voltage", and by measurements of the open circuit voltage decay and rise. Further evidence of the improved electrode is provided *via* the current density *vs.* voltage measurements in the dark. These show that Mg doping enables a decrease in the current leakage with a corresponding increase in the shunt resistance. Furthermore, Hall measurements indicate that Mg doping of ZnO ETLs increases the concentration of charge carriers in the ETL. The reason behind the hindering of performance with excess addition of Mg dopant (≈5%) in the ZnO ETL, is also discussed.

Experimental

Device fabrication

Materials. For the investigations, we have used the following widely available commercial materials: poly[4,8-bis(5-(2-ethylhexyl)thiophen-2-yl)benzo[1,2-*b*:4,5-*b*0]dithiophene-2,6-diyl-*alt*-(4-(2-ethylhexyl)-3-fluorothieno[3,4-*b*]thiophene-)-2-carboxylate-2-6-diyl)] (PTB7-Th), [6,6]-phenyl-C71-butyric acid methyl ester ($PC_{70}BM$), poly[(2,6-(4,8-bis(5-(2-ethylhexyl-3-fluoro)thiophen-2-yl)-benzo[1,2-b:4,5-*b*′]dithiophene))-*alt*-(5,5-(1′,3′-di-2-thienyl-5′,7′-bis(2-ethylhexyl)benzo[1′,2′-*c*:4′,5′-*c*′]dithiophene-4,8-dione)] (PM6) and 2,2′-((2Z,2′Z)-((12,13-bis(2-ethylhexyl)-3,9-diundecyl-12,13-dihydro-[1,2,5]thiadiazolo[3,4-e]thieno [2″,3′:4′,5′]thieno[2′,3′:4,5]pyrrolo[3,2-g]thieno[2′,3′:4,5] thieno [3,2-*b*]indole-2,10-diyl)bis(methanylylidene))bis(5,6-difluoro-3-*oxo*-2,3-dihydro-1*H*-indene-2,1-diylidene))dimalononitrile (Y6). The above materials were purchased from Ossila. Zinc acetate dihydrate, 2-methoxyethanol, ethanolamine, magnesium acetate tetrahydrate, 1-chloronaphthalene, chloroform, acetone and isopropanol were purchased from Sigma Aldrich. Chlorobenzene was purchased from Acros organics and 1,8-diiodooctane was purchased from Alfa Aesar. Evaporation materials Au and MoO_3 were purchased from Kurt J. Lesker. Glass/ITO substrates were purchased from Ossila.

Preparation of solutions. The PTB7-Th : $PC_{70}BM$ blend solution was formed by initially dissolving 15 mg of PTB7-Th in 1.5 mL chlorobenzene mixed with 45 μL of 1,8-diiodooctane. The solution was stirred at 70 °C for 4 hours. Then 22.5 mg of $PC_{70}BM$ were added to yield a 25 mg mL^{-1} concentration with blend ratio of 1 : 1.5. The solution was then allowed to stir overnight at room temperature. The PM6:Y6 blend solution was formed by dissolving 8 mg of PM6 and 9.6 mg of Y6 in 1.1 mL of chloroform to yield a 16 mg mL^{-1} concentration with blend ratio of 1 : 1.2. 1-Chloronaphthalene was added to the solution as a solvent additive (0.5%, v/v). The solution was then allowed to stir overnight at room temperature. All the above processes were carried out in a glovebox under a nitrogen environment. The various Mg-doped ZnO precursor solutions were formed by dissolving 0.1 g of a mixture of magnesium acetate tetrahydrate and zinc acetate dihydrate (with mass ratios of 0 : 100, 0.5 : 100, 1 : 100, 3 : 100, 5 : 100) along with 28 μL of ethanolamine in 1 mL of 2-methoxyethanol. The solutions were then stirred vigorously for 12 hours at room temperature.

Device fabrication. Glass/ITO substrates were cleaned in an ultra-sonicator, using soapy water, acetone and isopropanol for 10 minutes in each case. The substrates were then dried with a nitrogen spray gun and treated for 10 minutes in an oxygen plasma. The ≈30 nm thick ETL was then formed by spin-coating the ETL precursor solution on top of the substrate at 3000 revolutions per minute (rpm) for 30 seconds, followed by 1 hour annealing at 150 °C (or 300 °C for studies reported in the ESI‡) in air. Samples were then transferred to a nitrogen glovebox for the deposition of the active layer that was deposited *via* spin-coating. When PTB7-Th : $PC_{70}BM$ was employed, this

was deposited at 670 rpm for 60 seconds. When PM6-Y6 was employed this was deposited at 3800 rpm for 60 seconds and following the spin-coating the PM6:Y6 layer was annealed inside the glovebox at 80 °C for 5 minutes. After the formation of the active layer, samples were masked and loaded into a thermal evaporator (also housed in the nitrogen glovebox) evacuated to a residual pressure of 1.6×10^{-6} mbar before evaporation. A 9 nm thick MoO_3 layer was thermally evaporated with a rate of 0.1 Å s^{-1}. This was followed by thermal evaporation of 80 nm of Au at a rate of 0.2 Å s^{-1}. The active area of the devices is 4.5 mm^2. The OPV devices were completed by encapsulation with an epoxy resin and glass cover slips and by application of electrical connection legs. For the X-ray photoelectron spectroscopy (XPS), UPS, AFM, Kelvin probe, optical transmittance and DC Hall measurements, samples were prepared by following the exact same recipe detailed above up to the point before the deposition of the active layer. For part of the AFM and transmittance investigations the blend layer was deposited as well. For the transmittance measurements, ETLs were formed on a glass substrate without ITO.

Device characterisation

Current density–voltage & external quantum efficiency measurements. Current density–voltage characteristics under illumination and in darkness were obtained using a Keithley 2400 source-measure-unit (SMU) and a class AAA solar simulator (ABET Technologies, model Sun 3000 11016A). For measurements under illumination, the output of the lamp was calibrated to 1 sun using a standard Si photodetector. The J_{SC}, V_{OC}, FF and PCE were extracted from the current density *vs.* voltage characteristics. Dark curves were analysed further to extract the shunt resistance (R_{sh}). EQE spectra were obtained using a home-built system that uses a monochromated xenon lamp. The power density is extracted *via* the use of a calibrated Bentham DH-Si photodiode connected to an amplifier, while the current density output from the tested device is recorded with a Keithley 2400 SMU. To extract the calculated short circuit current density of devices the typical 1 sun spectrum was used. Masking of contacts was used as appropriate.

Open circuit voltage decay and rise. Open circuit voltage rise/decay measurements were performed using a Tektronix TD oscilloscope. The aforementioned solar simulator was used for switching the light intensity from the dark to 1 sun.

Optical transmittance. Transmission measurements were carried out by using an Agilent 8453 UV-vis spectrophotometer. The measurements for deposited ETLs were corrected by subtracting the spectrum of the corresponding glass substrate measured prior to ETL deposition.

Atomic force microscopy measurements. AFM images were captured with a Bruker Dimension Icon atomic force microscope, in peak force tapping mode with a ScanAsyst® cantilever (Bruker). Images were then analysed using Gwyddion. The uncertainty on the root mean square roughness is the standard deviation calculated on a set of two areas (of size 1.6 μm × 1.6 μm) on two different samples of each type.

Kelvin probe measurements. We used a Besocke DeltaPhi Kelvin probe for measuring the contact potential difference of samples. Measurements were performed in darkness. The results were corrected by using as reference a freshly-cleaved highly oriented pyrolytic graphite (HOPG) sample that has a known work function of 4.475 ± 0.005 eV.

XPS and UPS. XPS was performed in a JEOL JPS-9030 photoelectron spectrometer system using the Al Kα (1486 eV) excitation source (a monochromator was employed). The samples were grounded during the photoemission measurements. UPS was performed in an Omicron system equipped with a hemispherical energy analyzer (SPECS Phoibos 100) using the He I emission (21.2 eV) as excitation source with an 80% intensity aluminium filter. The samples were grounded during the measurements of the valence band region while a bias of −10 V was applied to the samples during the measurements of the work function calculated through the secondary electron cut off.

Hall measurements. Van der Pauw and Hall measurements were carried out on a Lakeshore 8404 Hall Measurement System. Contacts were confirmed ohmic (linear *I–V* plot, $t > 0.999$) prior to carrying out any measurements. The Van der Pauw technique was used to obtain film sheet resistance. Hall measurements were carried out using a DC magnetic field of 1 T.

Results and discussion

Formation of the Mg-doped ZnO electron transport layers

To form the Mg-doped ZnO ETLs, the ratio of magnesium acetate tetrahydrate to zinc acetate dihydrate precursors used in the precursor solution of the ETL is varied to influence the amount of Mg doping in the ETL. 5 Different precursor mass ratios were tested in the range of 0–5 : 100, namely 0 : 100 (undoped ZnO device), 0.5 : 100, 1 : 100, 3 : 100 and 5 : 100. To confirm that our experimental protocol yields the stoichiometrically predicted ratio of Zn to Mg in the finalised films, thin

Table 1 Ratio of Zn : Mg content in the Mg-doped ZnO ETLs containing different amounts of the Mg dopant and the resulting doping level. The abbreviations Prec. and Stoic. are used for the words precursor and stoichiometric. The last column shows the ratio of Mg atoms to the sum of Mg and Zn atoms in each sample

ETL (MgO : ZnO)	Prec. mass ratio Zn : Mg	Stoic. atom ratio Zn : Mg	XPS ratio of Zn : Mg	Stoic. Mg doping level (%)
(0.5 : 100)	200.0	195.4	100.8	0.51
(1 : 100)	100.0	97.7	77.2	1.01
(3 : 100)	33.3	32.6	34.3	2.98
(5 : 100)	20.0	19.5	18.4	4.87

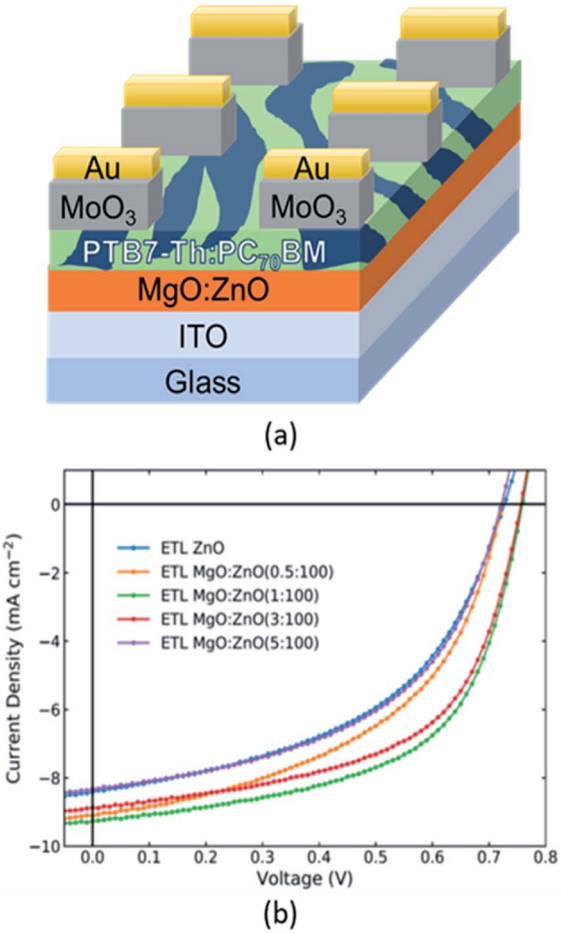

Fig. 1 (a) Schematic of the multi-layered structure of the OPV device. 5 Types of OPVs were tested, 4 with ETLs containing different amounts of Mg-doping in ZnO and an undoped "control" device. (b) Representative current density *vs.* voltage curves under 1 sun. Corresponding average key performance indicators from 8 distinct devices for each type of ETL are reported in Table 2.

films of ITO/ETL with the aforementioned precursor ratios were characterised with XPS (see Fig. S1 and Table S1‡). In Table 1 we demonstrate that for the selected precursor materials, the precursor mass ratio results in a similar stoichiometric atomic ratio of Zn : Mg (and corresponding Mg doping level) in the ETLs. The ratio of the Zn atomic signal divided by the Mg atomic signal as obtained from XPS (evaluated by the area of the Zn 2p and Mg 1s core level peaks) matches the stoichiometry atomic ratios of Zn : Mg expected from the precursors used to form the ETL solutions within ≈20%. The 0.5 : 100 sample exhibits a larger deviation between XPS and stoichiometric prediction. We attribute such a discrepancy to the measurement uncertainty resulting from the weak XPS signal for the film containing a minute amount of Mg and to the difficulty of adding the exact weight of magnesium acetate tetrahydrate precursor, when measuring in the sub-milligram region. Having confirmed that the films have the expected amounts of doping, we employ them as ETLs in inverted OPVs as shown by the schematic in Fig. 1a.

Table 2 Extracted parameters for OPV devices presented in Fig. 1. J_{SC} values were cross-checked with integrated EQE (see Table S2)

ETL (MgO : ZnO)	PCE (%)	J_{SC} (mA cm^{-2})	V_{OC} (mV)	FF
ZnO	3.21 ± 0.07	8.46 ± 0.04	736 ± 1	0.52 ± 0.01
(0.5 : 100)	3.32 ± 0.07	8.99 ± 0.04	721 ± 1	0.51 ± 0.01
(1 : 100)	3.79 ± 0.07	9.05 ± 0.04	742 ± 1	0.56 ± 0.01
(3 : 100)	3.71 ± 0.07	8.80 ± 0.04	739 ± 1	0.57 ± 0.01
(5 : 100)	3.08 ± 0.07	8.44 ± 0.04	734 ± 1	0.50 ± 0.01

Photovoltaic performance of Mg-doped ZnO based organic photovoltaics

The current density–voltage characteristics at 1 sun for PTB7-Th : $PC_{70}BM$ OPVs employing the undoped ZnO ETL *vs.* the Mg-doped ZnO ETLs with varying Mg content are shown in Fig. 1b. The corresponding average key PV performance indicators are displayed in Table 2. The results confirm that an enhancement in the efficiency of OPVs can be achieved by doping the ZnO ETL with Mg, *via* the direct addition of the MgO precursor to the ZnO precursor solution to form a single composite ETL using an annealing temperature of 150 °C. The best performing device employing the Mg-doped ZnO ETL was formed from a MgO : ZnO precursor ratio of 1 : 100 and has a relative increase in PCE of ≈18% with respect to the control device employing the undoped ZnO ETL. This is a consequence of an increase in the J_{SC}, V_{OC} and FF. The device with the ETL formed from a MgO : ZnO precursor ratio of 5 : 100, is exhibiting lower PCE than the undoped ZnO control. As the Mg content increases in the doped ZnO ETLs, the J_{SC} and FF of the devices increase, reaching a peak value in the region of 1–3% Mg doping level. The values of J_{SC} and FF then decrease with additional Mg doping. For the V_{OC} there are slight variations between the devices, but similarly, the highest V_{OC} is achieved at 1–3% doping. These results are consistent with findings for Mg-doped ZnO ETLs formed with an annealing temperature of 150 °C that were applied to perovskite PVs.[56] The results reported herein demonstrate that this strategy can be viable in the case of OPVs as well. Further testing in a sub-divided region of 1–3% Mg doping can be used to obtain an "optimised" doping level. The applicability of the Mg-doped ZnO ETLs has also been tested and shown to be successful for the case where the non-fullerene acceptor PM6:Y6 system has been used as the active layer in OPV devices (see Fig. S2, Tables S3 and S4‡). Similarly, the optimum Mg-doping is found to be in the region of ≈1–3%.

To identify the possible reasons behind the observed trends, thin films of the undoped ZnO ETL as well as films of the Mg-doped ZnO ETLs formed from MgO : ZnO precursor ratios of 1 : 100 and 5 : 100 (that exhibited the biggest variations in OPV performance) have undergone further physical and optical characterisation. In addition, the corresponding OPV devices have been subject to further electrical testing.

It is important to note that the optimum doping level range for the ETL is dependent on the annealing temperature employed. To demonstrate this, we have also tested OPVs containing ETLs formed with an annealing temperature of 300 °C (see Fig. S3 and Table S5‡). The OPV devices employing the

undoped ZnO ETL and the ETL formed from a MgO : ZnO precursor ratio of 1 : 100 show better performance when the ETL is annealed at 150 °C rather than 300 °C. At 300 °C the optimum Mg-doping is no longer in the range 1–3%.

As OPV devices approach commercial application, an increasingly important property to test for is stability. To test for stability, devices were measured on the day of fabrication and then kept under identical conditions before re-measurement after 45 days. The percentage decrease in PCE when re-measuring devices was 16.2% for the device containing the undoped ZnO ETL *vs.* 13.3% and 8.1% for the devices with ETLs formed from MgO : ZnO precursor ratios of 1 : 100 and 5 : 100 respectively. Therefore the presence of Mg is favourable in terms of device stability as well.

Characterisation of Mg-doped ZnO electrodes

UPS and Kelvin probe. To investigate the possible influence of Mg doping on the energetics of devices, the thin films were characterised with UPS, to extract the valence band onset and secondary electron cut-off (from which the work function is determined) (see Fig. S4‡). To cross reference the findings with regards to the work function, a Kelvin probe was also used to measure the contact potential difference with respect to a gold reference electrode. The results are summarised in Table 3. We attribute the minor discrepancies in the absolute values of work function obtained from UPS and Kelvin probe to the rather different measurement environments, and to the fact that the minimum value of the work function is measured with UPS, whereas Kelvin probe measurements yield a value averaged over the area of the electrode.[61] In any case, both techniques are suitable in detecting changes in work function between two samples that have been prepared under the same conditions. Within the tested doping region both the UPS and Kelvin probe measurements show that the work function value remains constant. Mg-doping has been shown to alter the work function or conduction and valence band levels of electrodes but there are some conflicting reports on this issue.[58,59] In this study, due to the limited amount of doping (<5%), no change is observed in these parameters. Therefore, it is unlikely that the performance changes observed in the PV measurements, relate to the tuning in the energetics of the device.

Table 3 Work function measurements from Kelvin probe and UPS investigations, and valence band onset. No significant variation in the energetics of the device is observable

ETL (MgO : ZnO)	Φ (eV) (Kelvin Probe)	Φ (eV) (UPS)	VB onset (eV)
ZnO	4.2 ± 0.1	3.6 ± 0.1	3.6 ± 0.1
(1 : 100)	4.1 ± 0.1	3.6 ± 0.1	3.6 ± 0.1
(5 : 100)	4.1 ± 0.1	3.7 ± 0.1	3.6 ± 0.1

Atomic force microscopy. We investigated potential variations in the surface morphology and root mean square roughness (Sq) of the PTB7-Th : $PC_{70}BM$ blend on top of the undoped and Mg-doped ZnO ETLs, *via* tapping mode AFM and we report the corresponding images in Figure 2(a–c). There are only insignificant variations in Sq between the films (smaller than the uncertainties), hence, it can be inferred that for the length

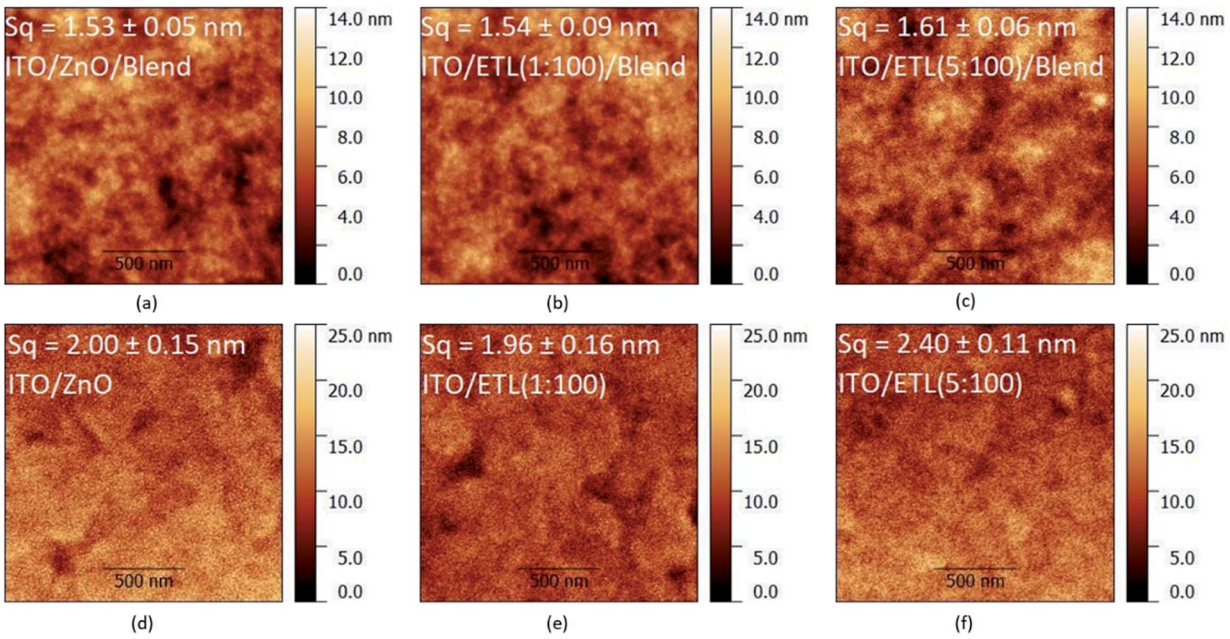

Fig. 2 Tapping mode AFM images (1.6 μm × 1.6 μm, annotated with the corresponding root mean square roughness (Sq)) of the topography of (a) ITO/ZnO/PTB7-Th : $PC_{70}BM$, (b) ITO/Mg-doped (1 : 100) ZnO/PTB7-Th : $PC_{70}BM$, (c) ITO/Mg-doped (5 : 100) ZnO/PTB7-Th : $PC_{70}BM$, (d) ITO/ZnO, (e) ITO/Mg-doped (1 : 100) ZnO and (f) ITO/Mg-doped (5 : 100) ZnO. There is no significant variation of Sq between the bare ITO/ZnO and ITO/Mg-doped (1 : 100) ZnO films, although Sq is ≈20% larger for the (5 : 100) MgO : ZnO films. Mg-doping of the ETL does not influence the morphology of the PTB7-Th : $PC_{70}BM$ blend for the investigated length scales.

Table 4 Hall measurements. The Hall mobility, carrier concentration and resistivity values were extracted from the measurement

ETL (MgO : ZnO)	Hall mobility ($cm^2\ V^{-1}\ s^{-1}$)	Carrier concentration ($\times 10^{21}\ cm^{-3}$)	Resistivity ($\times 10^{-5}\ \Omega$ cm)
ZnO	39.8 ± 0.05	1.86 ± 0.03	8.44 ± 0.01
(1 : 100)	34.8 ± 0.05	2.00 ± 0.11	8.97 ± 0.01
(5 : 100)	40.9 ± 0.05	2.03 ± 0.06	7.51 ± 0.01

scales investigated here, Mg-doping of the ETL does not influence the morphology of the blend. We report the AFM images of the corresponding ETL films without the blend on top in Fig. 2d–f respectively for the different Mg loadings. The variation in Sq between the ETL formed from a MgO : ZnO precursor ratio of 1 : 100 and the undoped ZnO ETL is smaller than the uncertainties in the measurements, however, there is $a \approx 20\%$ increase in Sq for the ETL formed from a MgO : ZnO precursor ratio of 5 : 100. Such an increase in Sq is indicative of a less uniform and less homogeneous surface of the ETL at ≈5% loading, with potential phase separation and formation of MgO-rich regions which may influence negatively the OPV performance (*vide infra*).

Hall measurements. The van der Pauw method was used to assess the electrical properties of the films. The extracted parameters from the measurement are shown in Table 4. Mg doping leads to a higher carrier concentration in the thin films. In general, Hall mobility is expected to decrease with doping due to enhanced scattering (as seen in the case of Si doping for example). Hence the film formed from the MgO : ZnO precursor ratio of 1 : 100 exhibits a lower Hall mobility than the undoped ZnO film. The film formed from the MgO : ZnO precursor ratio of 5 : 100, even though expected to show an even lower Hall mobility, exhibits a Hall mobility that it is very similar to the undoped ZnO thin film. This might be the result of a potential phase separation between ZnO and MgO that appears to occur for this higher level of Mg doping, as suggested by the rougher morphology of these films observed in the AFM investigation. The resistivity of a film is proportional to the inverse of the product of carrier concentration and mobility. This leads to the highest resistivity obtained when the ETL is formed from the MgO : ZnO precursor ratio of 1 : 100.

Optical spectroscopy. To assess the effect of Mg doping on the optical properties of the ETLs, transmission measurements were carried out as shown in Fig. 3 (for further clarity, the same data are plotted in terms of absorbance with corresponding Tauc plots in Fig. S5‡). The Mg-doped ZnO ETLs show slightly increased transmittance compared to the undoped ZnO ETL in the region of 325–400 nm. The observed blue shift with increasing Mg content, is consistent with previous literature,[59] however the shift is not very significant (≈9 nm), a circumstance that we attribute to the Mg doping being minimal. We also carried out transmission measurements on the films after the deposition of a PTB7-Th : $PC_{70}BM$ or PM6:Y6 blend layer on top of the undoped and Mg-doped ZnO ETLs (see Fig. S6‡). The samples incorporating the Mg-doped ZnO show a slightly increased transmittance (≈8% in relative terms) throughout the tested spectral region (300–900 nm). The increase in J_{SC} observed in the OPV devices is thus not associated with increased absorption in the active layer blend.

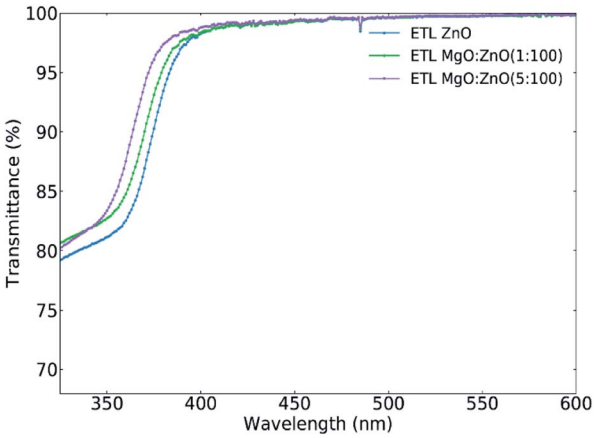

Fig. 3 Transmission spectra of thin films of ZnO and Mg-doped ZnO. There is a blue-shift in the spectrum with increasing Mg-doping.

Electrical characterisation of Mg-doped ZnO OPV devices. Fig. 4 reports a collection of further electrical characterisations carried out on the PTB7-Th : $PC_{70}BM$ based OPV devices. For the corresponding figure of the PM6:Y6 based OPV devices see Fig. S7.‡ The incremental addition of Mg in the ZnO ETL leads to a corresponding reduction in the current leakage in the OPV device. This is evidenced in Fig. 4a (Fig. S7a‡), where the (dark) current *vs.* voltage characteristics of the OPV diodes are shown. This reduced leakage is indicative of an increased shunt resistance (see Fig. S8‡). The average current density at −1 V is -1.41×10^{-3} mA cm^{-2} for the undoped ZnO ETL and decreases to -3.31×10^{-4} mA cm^{-2} for the Mg-doped ZnO ETL device formed from a MgO : ZnO precursor ratio of 1 : 100 and further decreases to -1.18×10^{-4} mA cm^{-2} for the Mg-doped ZnO ETL device formed from a MgO : ZnO precursor ratio of 5 : 100. A corresponding increase in R_{sh} is observed, with R_{sh} calculated as $4.35 \times 10^6\ \Omega\ cm^2$, $1.17 \times 10^7\ \Omega\ cm^2$ and $1.42 \times 10^7\ \Omega\ cm^2$ respectively. A similar trend is observed in the corresponding average current density at −1 V and resulting R_{sh} values for the PM6:Y6 devices as well (see Table S6‡). To gain further insight in the extraction properties and the recombination in these devices, we have investigated the dependence of the photocurrent density (J_{PH}) on the effective voltage (V_{EFF})[62] and measured the decay and rise times of the V_{OC}. The J_{PH} and V_{EFF} can be calculated using the expressions $J_{PH} = |J_L - J_D|$ and $V_{EFF} = V_0 - V_a$ where J_L and J_D are the measured photocurrents under

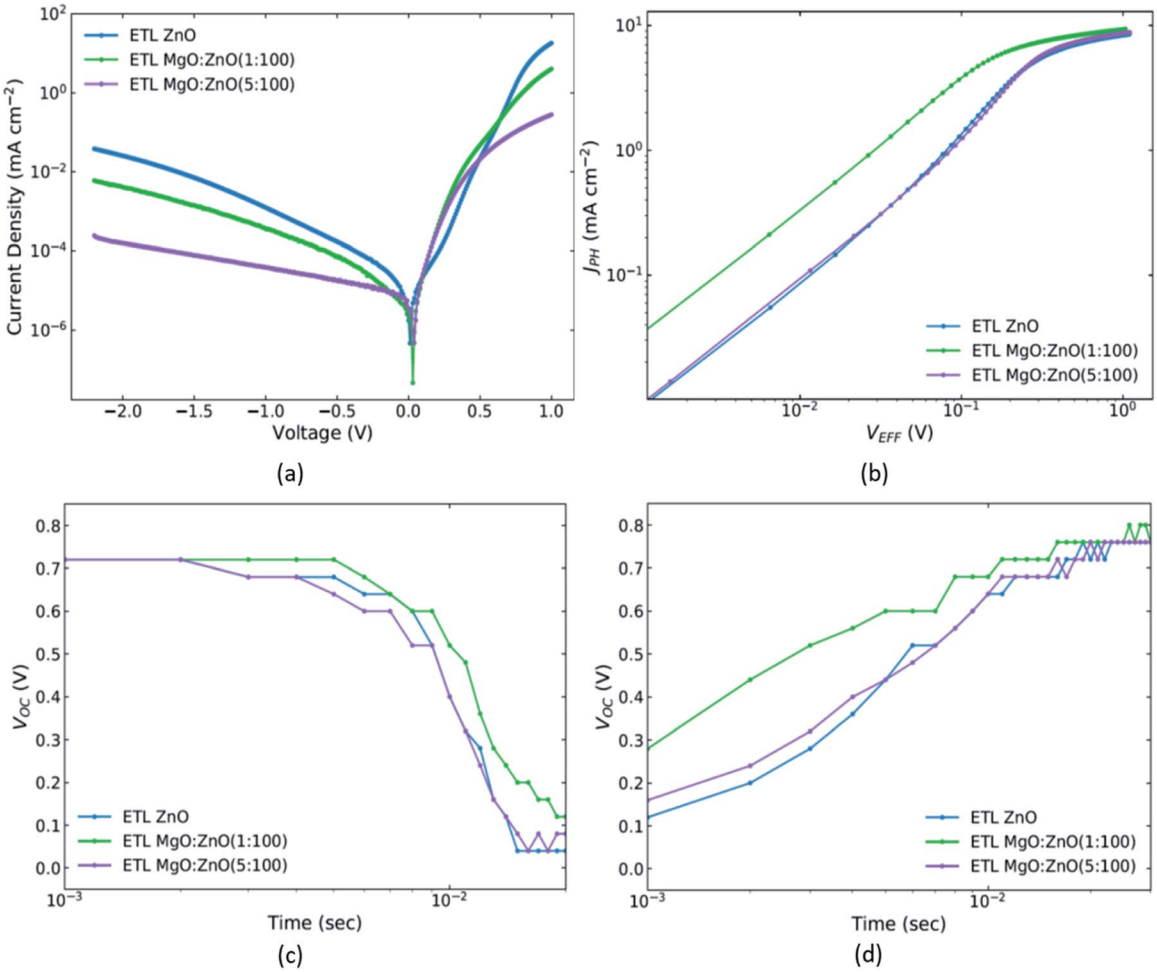

Fig. 4 (a) Current density–voltage curves in the dark. (b) Photocurrent density–effective voltage curves. (c) Open circuit voltage decay curves (in the dark). (d) Open circuit voltage rise curves (under 1 sun).

illumination and in the dark respectively, V_a is the externally applied voltage and V_0 is the (externally applied) voltage at $J_{PH} = 0$. Fig. 4b (Fig. S7b‡) shows the variation of the J_{PH} with V_{EFF}. As expected from the PV characterisation, the Mg-doped ZnO ETL device formed from a MgO : ZnO precursor ratio of 1 : 100 shows the best performance. The extraction of J_{PH} at saturation ($J_{PH,SAT}$) which occurs at high V_{EFF} (~1.1 V where the device in reverse bias) as well its extraction at short circuit ($J_{PH,SC}$) allow for the calculation of an indicator that can be used to quantify the variation in performance of the devices with differing Mg doping. Such an indicator is the ratio $J_{PH,SC}/J_{PH,SAT}$ (P_{DISS}) which some authors consider akin to the relative exciton dissociation efficiency.[31,32,36] We note in this regard that since such a parameter is calculated as a ratio of collected currents it will not account for any recombination event taking place even at the strongest fields applied "in saturation" (as specified above). It does however provide information on the effectiveness with which dissociated excitons are extracted. We find P_{DISS} increases from 95.85% for the undoped ZnO device to 96.76% for the 1 : 100 Mg-doped ZnO device before decreasing to 95.83% at 5 : 100 Mg loading. Similarly, for the case of PM6:Y6 devices, P_{DISS} increases from 94.88% for the undoped ZnO device to 95.72% for the 1 : 100 Mg-doped ZnO device before decreasing to 94.37% at 5 : 100 Mg loading. Finally, Fig. 4c and d (Fig. S7c and S7d‡), demonstrate the time dependent V_{OC} decay and rise for the OPV devices. The OPV device based on the Mg-doped ZnO ETL formed from a MgO : ZnO precursor ratio of 1 : 100 takes the longest time to be completely discharged in comparison to the other devices. This also holds for the PM6:Y6 based OPVs. In addition, it requires a shorter rise time to arrive at the maximum V_{OC} (for PM6:Y6 rise times are similar between the undoped ZnO device and the 1 : 100 Mg-doped ZnO device and slower for the 5 : 100 doped ZnO device). The trends observed in the open circuit voltage and decay studies are indicative of reduced recombination in the 1 : 100 Mg-doped ZnO device.[63,64]

Discussion

The results above show that low-temperature annealing of a mixed MgO : ZnO precursor leads to a significant increase of the performance parameters of OPVs incorporating such an ETL, and in particular an ≈18% relative increase of the PCE

with respect to undoped ZnO ETLs for films with $a \approx 1\%$ atomic Mg doping.

Interestingly, analysis of the electrical properties of the OPVs reveal a higher shunt resistance (accounting for the reduced losses for such devices, also evidenced by the faster increase of the V_{OC} upon light switch-on and the slower V_{OC} decay after light switch-off, as well as by the decreased dark current in reverse bias (Fig. 4a)). The increased J_{PH} on the other hand (Fig. 4b) indicates a reduction in the series resistance (R_s) which would also lead to an increase of both the J_{SC} and of the FF, as indeed observed. Of course, the increased R_{sh} also accounts for the increased V_{OC}, and J_{SC}.

To gather some insight into the microscopic origin of such loss reductions we note that the properties of ZnO films are well-established to be highly dependent on the presence and/or concentration of defects such as oxygen vacancies, zinc interstitials and/or other dopants.[65] For example, it has been proposed that Mg can reduce the density of oxygen vacancies in ZnO nanorods.[66] In our case as well, we suggest that Mg doping compensates oxygen vacancies which may act as charge recombination centres. In addition, we note that bulk MgO is characterised by a rather large ionisation potential (~10 eV) compared to ZnO (~7.6 eV), thereby suggesting significantly better hole-blocking properties for any MgO-rich region of the modified electrodes, which would also contribute to reduction of PV losses linked to hole currents flowing through the electron-collecting electrode.

The question arises as to how much Mg will provide optimum results. Our data show that the best results are obtained with a Mg loading between ≈1 and 3%, but that when increasing this to ≈5%, despite a higher R_{sh} (expected for the more insulating nature of MgO) carrier recombination becomes significant (*e.g.* from Fig. 4c and d) eventually leading to a lower PCE. It is interesting that the Hall (lateral) resistivity at ≈5% Mg is decreased with respect to undoped and ≈1%-doped ETLS, with a concomitant increase of the electron mobility, thereby hinting at a potential overcompensation of the oxygen vacancies, with a concomitant increase of carrier recombination centres. This is also corroborated by the morphology changes visible in AFM images at such a concentration (Fig. 2).

In summary we propose that ≈1% Mg doping strikes the "right balance" between the various processes at play, *i.e.*, extraction of the electrons, blocking of the holes and hole–electron recombination.

Conclusions

We have shown that Mg acetate can be directly added to ZnO precursor solutions to form Mg-doped ZnO ETLs for OPVs with a reduced annealing temperature of 150 °C. Not only is this appealing for low-temperature industrial manufacturing and greater sustainability, but also affords greater OPV PCEs. We obtained our best results with a 1 : 100 MgO : ZnO precursor concentrations and this yields a relative increase in efficiency of ≈18% compared to devices incorporating undoped ZnO ETLs. This exceeds the relative improvement in efficiency we have previously reported (≈10%) when MgO was used on top of ZnO (*i.e.* effectively forming a bilayer). The increase in PCE observed in this work, is a result of an enhanced J_{SC}, V_{OC} and FF, which we can trace down to an improved contact with the active layer exhibiting a decreased recombination and leakage current. Doping with low levels of Mg does not significantly affect the work function or blend morphology. Our results show that for achieving better performance the Mg doping needs to be limited when the annealing temperature used is 150 °C, as doping in the ETL formed from a MgO : ZnO precursor ratio of 5 : 100 is already excessive and can hinder performance. The Mg-doped devices show enhanced stability and this strategy is viable for OPVs based both on fullerene and non-fullerene acceptor active layer blends. Our work provides an industrially scalable approach to electrodes for high-performance OPVs and is in principle applicable to both top and bottom contact electrodes.

Conflicts of interest

There are no conflicts to declare.

Acknowledgements

Special thanks to Natalie Stingelin and Marcello Righetto for useful discussions. We acknowledge use of the London Centre for Nanotechnology Atomic Force Microscope Facility. I. I. was supported by the EPSRC and SFI Centre for Doctoral Training in Advanced Characterisation of Materials (Grant Ref: EP/L015277/1). G. L. and E. L.-K. thank Professor N. Koch (HU Berlin) for granting access to photoemission tools, DFG (Project No. 182087777-SFB 951) and the HySPRINT Innovation Lab at Helmholtz-Zentrum Berlin (through the framework of the Joint Lab GEN_FAB) for financial support. K. G. acknowledges funding from the Royal Society through a Newton International Fellowship. F. C. thanks EPSRC for financial support *via* grant EP/P007767/1.

Notes and references

1 G. M. Lazzerini, F. Di Stasio, C. Flechon, D. J. Caruana and F. Cacialli, *Appl. Phys. Lett.*, 2011, **99**, 243305.
2 N. S. Lewis and D. G. Nocera, *Proc. Natl. Acad. Sci. U. S. A.*, 2007, **103**, 15729–15735.
3 C. J. Brabec, A. Distler, X. Y. Du, H. J. Egelhaaf, J. Hauch, T. Heumueller and N. Li, *Adv. Energy Mater.*, 2020, **10**, 2001864.
4 J. Barsotti, A. G. Rapidis, I. Hirata, F. Greco, F. Cacialli and V. Mattoli, *Adv. Electron. Mater.*, 2021, **7**, 2001145.
5 I. Ierides, A. Zampetti and F. Cacialli, *Curr. Opin. Green Sustainable Chem.*, 2019, **17**, 15–20.
6 L. Kinner, T. Dimopoulos, G. Ligorio, E. J. W. List-Kratochvil and F. Hermerschmidt, *RSC Adv.*, 2021, **11**, 17324–17331.
7 P. W. M. Blom, *Adv. Mater. Technol.*, 2020, **5**, 2000144.
8 R. Sorrentino, E. Kozma, S. Luzzati and R. Po, *Energy Environ. Sci.*, 2021, **14**, 180–223.
9 Z. Yin, J. Wei and Q. Zheng, *Adv. Sci.*, 2016, **3**, 1500362.

10 M. Graetzel, R. A. J. Janssen, D. B. Mitzi and E. H. Sargent, *Nature*, 2012, **488**, 304–312.
11 K. Mahmood, S. Sarwar and M. T. Mehran, *RSC Adv.*, 2017, **7**, 17044–17062.
12 H. L. Yip and A. K. Y. Jen, *Energy Environ. Sci.*, 2012, **5**, 5994–6011.
13 C. Y. Chan, Y. F. Wei, H. T. Chandran, C. S. Lee, M. F. Luo and T. W. Ng, *RSC Adv.*, 2015, **5**, 77071–77074.
14 J. C. D. Faria, A. J. Campbell and M. A. McLachlan, *Adv. Funct. Mater.*, 2015, **25**, 4657–4663.
15 Z. Liang, Q. Zhang, L. Jiang and G. Cao, *Energy Environ. Sci.*, 2015, **8**, 3442–3476.
16 J. C. Wang, W. T. Weng, M. Y. Tsai, M. K. Lee, S. F. Horng, T. P. Perng, C. C. Kei, C. C. Yu and H. F. Meng, *J. Mater. Chem.*, 2010, **20**, 862–866.
17 J. B. Franklin, B. Zou, P. Petrov, D. W. McComb, M. P. Ryan and M. A. McLachlan, *J. Mater. Chem.*, 2011, **21**, 8178–8182.
18 A. Rivera, A. Mazady, K. Ahi and M. Anwar, *Proc. SPIE*, 2015, **9483**, 948301–948307.
19 S. Schumann, R. Da Campo, B. Illy, A. C. Cruickshank, M. A. McLachlan, M. P. Ryan, D. J. Riley, D. W. McComb and T. S. Jones, *J. Mater. Chem.*, 2011, **21**, 2381–2386.
20 Y. Lin, Y. Firdaus, M. I. Nugraha, F. Liu, S. Karuthedath, A. H. Emwas, W. Zhang, A. Seitkhan, M. Neophytou, H. Faber, E. Yengel, I. McCulloch, L. Tsetseris, F. Laquai and T. D. Anthopoulos, *Adv. Sci.*, 2020, **7**, 1903419.
21 X. Du, Y. Yuan, L. Zhou, H. Lin, C. Zheng, J. Luo, Z. Chen, S. Tao and L. S. Liao, *Adv. Funct. Mater.*, 2020, **30**, 1909837.
22 Y. Sun, J. H. Seo, C. J. Takacs, J. Seifter and A. J. Heeger, *Adv. Mater.*, 2011, **23**, 1679–1683.
23 J. Zhang, H. Yang, X. Zhang, M. Morbidoni, C. H. Burgess, R. Kilmurray, S. Feng and M. A. McLachlan, *Inorg. Chem. Front.*, 2020, **7**, 2809–2817.
24 J. Zhang, M. Morbidoni, C. H. Burgess, J. Wu, T. Du, K. Harrabi, D. J. Payne, J. R. Durrant and M. A. McLachlan, *Cryst. Growth Des.*, 2017, **17**, 6559–6564.
25 J. Zhang, J. C. D. Faria, M. Morbidoni, Y. Porte, C. H. Burgess, K. Harrabi and M. A. McLachlan, *Adv. Electron. Mater.*, 2016, **2**, 1600008.
26 X. Zhang, Y. Sun, M. Wang, H. Cui, W. Xie, L. Shen and W. Guo, *Sol. Energy*, 2019, **181**, 9–16.
27 T. M. Brown, G. M. Lazzerini, L. J. Parrott, V. Bodrozic, L. Burgi and F. Cacialli, *Org. Electron.*, 2011, **12**, 623–633.
28 I. Ierides, I. Squires, G. Lucarelli, T. M. Brown and F. Cacialli, *J. Mater. Chem. C*, 2021, **9**, 3901–3910.
29 M. Li, J. Li, L. Yu, Y. Zhang, Y. Dai, R. Chen and W. Huang, *Front. Chem.*, 2020, **8**, 399.
30 Y. Xia, C. Wang, B. Dong, G. Wang, Y. Chen, R. C. I. MacKenzie, W. Dong, S. Ruan, Y. Liu and S. Wen, *ACS Appl. Mater. Interfaces*, 2021, **13**, 14423–14432.
31 B. Guo, J. Han, J. Qiu, C. Yu, Y. Sun, F. Li, Z. Hu and Y. Wang, *ACS Appl. Mater. Interfaces*, 2017, **9**, 42969–42977.
32 C. Hou and H. Yu, *Chem. Eng. J.*, 2021, **407**, 127192.
33 S. Park, R. Kang and S. Cho, *Curr. Appl. Phys.*, 2020, **20**, 172–177.
34 B. Usmani, R. Ranjan, Prateek, S. K. Gupta, R. K. Gupta, K. S. Nalwa and A. Garg, *Sol. Energy*, 2021, **214**, 220–230.
35 D. Chi, S. Lu, R. Xu, K. Liu, D. Cao, L. Wen, Y. Mi, Z. Wang, Y. Lei, S. Qu and Z. Wang, *Nanoscale*, 2015, **7**, 15251–15257.
36 X. Song, G. Liu, P. Sun, Y. Liu and W. Zhu, *J. Phys. Chem.*, 2021, **12**, 10616–10621.
37 M. Wang, Y. Sun, J. Guo, Z. Li, C. Liu and W. Guo, *Org. Electron.*, 2019, **74**, 258–264.
38 M. Chrzanowski, M. Kuchowicz, R. Szukiewicz, P. Sitarek, J. Misiewicz and A. Podhorodecki, *Org. Electron.*, 2020, **80**, 105656.
39 H. M. Kim, S. Cho, J. Kim, H. Shin and J. Jang, *ACS Appl. Mater. Interfaces*, 2018, **10**, 24028–24036.
40 Y. Sun, Y. Jiang, H. Peng, J. Wei, S. Zhang and S. Chen, *Nanoscale*, 2017, **9**, 8962–8969.
41 L. Wang, J. Lin, X. Liu, S. Cao, Y. Wang, J. Zhao and B. Zou, *J. Phys. Chem. C*, 2020, **124**, 8758–8765.
42 H. M. Kim, W. Jeong, J. H. Kim and J. Jang, *Nanomaterials*, 2020, **10**, 2423.
43 L. Wang, J. Pan, J. Qian, W. Lei, Y. Wu, W. Zhang, D. K. Goto and J. Chen, *J. Mater. Chem. C*, 2018, **6**, 8099–8104.
44 M. M. Yan, Y. Li, Y. T. Zhou, L. Liu, Y. Zhang, B. G. You and Y. Li, *IEEE Photonics J.*, 2017, **9**, 8200508.
45 S. B. Heo, J. S. Shin, T. Y. Kim, S. Park, W. H. Jung, H. Kim, J. A. Hong, B. S. Kim, Y. Park, B. D. Chin, J. G. Kim and S. J. Kang, *Curr. Appl. Phys.*, 2021, **29**, 107–113.
46 H. Wu, Y. Zhang, X. Zhang, M. Lu, C. Sun, T. Zhang and W. W. Yu, *Adv. Opt. Mater.*, 2017, **5**, 1700377.
47 Y. J. Lin, P. H. Wu, C. L. Tsai, C. J. Liu, Z. R. Lin, H. C. Chang and C. T. Lee, *J. Appl. Phys.*, 2008, **103**, 113709.
48 G. El Hallani, S. Nasih, N. Fazouan, A. Liba, M. Khuili, M. Sajieddine, M. Mabrouki, L. Laanab and E. H. Atmani, *J. Appl. Phys.*, 2017, **121**, 135103.
49 A. Singh and P. Kumar, *J. Optoelectron. Adv. Mater.*, 2014, **16**, 311–316.
50 L. Meng, X. Yang, H. Chai, Z. Lv and T. Yang, *Thin Solid Films*, 2019, **672**, 186–191.
51 A. Ringleb, R. Ruess, N. Hofeditz, W. Heimbrodt, T. Yoshida and D. Schlettwein, *Phys. Chem. Chem. Phys.*, 2021, **23**, 8393–8402.
52 C. J. Raj, K. Prabakar, S. N. Karthick, K. V. Hemalatha, M. K. Son and H. J. Kim, *J. Phys. Chem. C*, 2013, **117**, 2600–2607.
53 I. Biswas, P. Roy, U. Maity, P. K. Sinha and A. K. Chakraborty, *Thin Solid Films*, 2020, **711**, 138301.
54 M. Xing, Y. Wei, D. Wang, Q. Shen and R. Wang, *Curr. Appl. Phys.*, 2021, **21**, 14–19.
55 J. Song, E. Zheng, L. Liu, X. F. Wang, G. Chen, W. Tian and T. Miyasaka, *Chemsuschem*, 2016, **9**, 2640–2647.
56 X. Li, J. Yang, Q. Jiang, W. Chu, J. Xin, J. Hou and H. Lai, *Electrochim. Acta*, 2018, **261**, 474–481.
57 R. T. Ginting, C. C. Yap, M. Yahaya and M. M. Salleh, *J. Alloys Compd.*, 2014, **585**, 696–702.
58 Z. Yin, Q. Zheng, S. C. Chen, D. Cai, L. Zhou and J. Zhang, *Adv. Energy Mater.*, 2014, **4**, 1301404.
59 B. A. MacLeod, P. Schulz, S. R. Cowan, A. Garcia, D. S. Ginley, A. Kahn and D. C. Olson, *Adv. Energy Mater.*, 2014, **4**, 1400073.

60 N. Johansson, F. Cacialli, K. Z. Xing, G. Beamson, D. T. Clark, R. H. Friend and W. R. Salaneck, *Synth. Met.*, 1998, **92**, 207–211.
61 J. S. Kim, B. Lagel, E. Moons, N. Johansson, I. D. Baikie, W. R. Salaneck, R. H. Friend and F. Cacialli, *Synth. Met.*, 2000, **111–112**, 311–314.
62 V. D. Mihailetchi, H. Xie, B. de Boer, L. J. A. Koster and P. W. M. Blom, *Adv. Funct. Mater.*, 2006, **16**, 699–708.
63 J. Dagar, S. Castro-Hermosa, G. Lucarelli, F. Cacialli and T. M. Brown, *Nano Energy*, 2018, **49**, 290–299.
64 J. Vollbrecht and V. V. Brus, *Energies*, 2021, **14**, 4800.
65 A. Janotti and C. G. Van de Walle, *Rep. Prog. Phys.*, 2009, **72**, 126501.
66 X. Yu, X. Yu, M. Yan, T. Weng, L. Chen, Y. Zhou and J. Wei, *Sens. Actuators, A*, 2020, **312**, 112163.